Atmos. Chem. Phys., 14, 12225–12236, 2014
www.atmos-chem-phys.net/14/12225/2014/
doi:10.5194/acp-14-12225-2014

Atmospheric Chemistry and Physics
Open Access

Cirrus and water vapour transport in the tropical tropopause layer – Part 2: Roles of ice nucleation and sedimentation, cloud dynamics, and moisture conditions

T. Dinh[1], **S. Fueglistaler**[1,2], **D. Durran**[2,3], **and T. Ackerman**[2,3]

[1]Program in Atmospheric and Oceanic Sciences, Princeton University, Princeton, NJ 08540, USA
[2]Department of Geosciences, Princeton University, Princeton, NJ 08540, USA
[3]Department of Atmospheric Sciences, University of Washington, Seattle, WA 98195, USA

Correspondence to: T. Dinh (tdinh@princeton.edu)

Received: 8 April 2014 – Published in Atmos. Chem. Phys. Discuss.: 22 May 2014
Revised: 22 September 2014 – Accepted: 3 October 2014 – Published: 20 November 2014

Abstract. A high-resolution, two-dimensional numerical model is used to study the moisture redistribution following homogeneous ice nucleation induced by Kelvin waves in the tropical tropopause layer (TTL). We compare results for dry/moist initial conditions and three levels of complexity for the representation of cloud processes: complete microphysics and cloud radiative effects, likewise but without radiative effects, and instantaneous removal of moisture in excess of saturation upon nucleation.

Cloud evolution and moisture redistribution are found to be sensitive to initial conditions and cloud processes. Ice sedimentation leads to a downward flux of water, whereas the cloud radiative heating induces upward advection of the cloudy air. The latter results in an upward (downward) flux of water vapour if the cloudy air is moister (drier) than the environment, which is typically when the environment is subsaturated (supersaturated).

Only a fraction ($\sim$25 % or less) of the cloud experiences nucleation. Post-nucleation processes (ice depositional growth, sedimentation, and sublimation) are important to cloud morphology, and both dehydrated *and* hydrated layers may be indicators of TTL cirrus occurrence. The calculation with instantaneous removal of moisture not only misses the hydration but also underestimates dehydration due to (i) nucleation before reaching the minimum saturation mixing ratio, and (ii) lack of moisture removal from sedimenting ice particles below the nucleation level.

The sensitivity to initial conditions and cloud processes suggests that it is difficult to reach generic, quantitative estimates of cloud-induced moisture redistribution on the basis of case-by-case calculations.

1 Introduction

Stratospheric water vapour plays an important role in the chemistry of the stratosphere (Solomon et al., 1986) and the radiation budget of the atmosphere (Forster and Shine, 2002; Solomon et al., 2010). Air enters the stratospheric overworld (terminology following Hoskins, 1991) predominantly across the tropical tropopause, where the exceptionally low temperatures limit the water vapour mixing ratios to a few parts per million (Brewer, 1949). However, the processes that control dehydration as air ascends across the tropical tropopause layer (TTL; see, for example, Fueglistaler et al., 2009; Randel and Jensen, 2013) into the stratosphere remain incompletely understood. The high frequency of occurrence (20 to 50 %) of thin cirrus clouds in the TTL (Wang et al., 1996; Mace et al., 2009; Virts et al., 2010) indicates that these clouds may be the last dehydration events for a substantial fraction of air entering the stratosphere.

Cirrus clouds in the TTL may form as remnants of outflow from deep convection (Massie et al., 2002; Wang and Dessler, 2012) or in situ, whereby transient temperature perturbations associated with tropical waves initiate cloud formation (Boehm and Verlinde, 2000; Immler et al., 2008; Fujiwara et al., 2009). The efficiency of the dehydration of the air that follows cloud formation remains not well quantified (see

Published by Copernicus Publications on behalf of the European Geosciences Union.

Dinh and Fueglistaler, 2014b, for estimates and uncertainties). Idealised model calculations that assume instantaneous dehydration to the saturation mixing ratio provide reasonable estimates of annual and interannual variabilities of water entering the stratosphere (Fueglistaler et al., 2005; Fueglistaler and Haynes, 2005; James et al., 2008), but may be systematically dry-biased (Liu et al., 2010). Calculations with microphysical box models of various complexity (Gettelman et al., 2002; Ren et al., 2007; Fueglistaler et al., 2013) or one-dimensional (time–height) models (Jensen and Pfister, 2004) show that incomplete gravitational removal of ice particles can reduce dehydration, but with the reduced dimensionality these models cannot capture the effects of shear, mixing, and cloud-scale circulations induced by the cloud radiative heating (see Durran et al., 2009; Dinh et al., 2010, 2012; Schmidt and Garrett, 2013; Dinh and Fueglistaler, 2014a).

Here, we study the moisture redistribution by thin cirrus clouds with a cloud-resolving model initialised and forced with idealised conditions typical for the TTL. This work follows up on a case modelling study by Dinh et al. (2012), who simulated a TTL cirrus cloud with characteristics similar to observations. Our objective here is to study how efficiently thin cirrus clouds dehydrate the air, and how the resulting moisture redistribution depends on the complexity of the physical processes resolved in the model. Towards this goal, we carry out three sets of model simulations, which are labelled "all physics" (all-phys), "no-radiation" (no-rad), and "infinite-sedimentation" (inf-sed). For the most complete all-phys simulations, cloud formation due to homogeneous ice nucleation and subsequent ice sedimentation are calculated with detailed bin microphysics. Furthermore, the dynamical perturbations induced by the radiative heating in the presence of ice crystals are taken into account. In the no-rad simulations, the cloud radiative effects are neglected. Finally, for the inf-sed simulations, we drastically simplify the microphysics by assuming that, upon nucleation, ice particles take up all moisture in excess of saturation and immediately sediment out of the domain (at an infinite fall speed).

The model results are analysed from an Eulerian perspective of domain average water vapour profiles, and from a Lagrangian perspective of air parcels. The Lagrangian perspective is often employed in idealised studies (e.g. Fueglistaler et al., 2013) and for interpretations of in situ observations (e.g. Inai et al., 2013). Our numerical results show how such interpretations may be affected by problems arising from incomplete modelling of the cloud processes.

The article is organised as follows. Sections 2 describes the model and configuration of the numerical experiments. Section 3.1 describes the evolution of the clouds in the simulations. The redistribution of moisture following the occurrence of the clouds is evaluated from the changes in water vapour in the Eulerian domain (Sect. 3.2), and as following air parcels (Sect. 3.3). Section 4 summarises the results and discusses the contribution of this research to the understanding of the dehydration problem in the TTL.

2 Model configuration

This section describes the model configuration of six numerical experiments, namely all-phys, no-rad, and inf-sed for two initial moisture profiles (dry/moist). The simulations are forced by the perturbations from a large-scale Kelvin wave and are integrated over one life cycle of a cloud. The simulations build on previous model development by Dinh et al. (2012), to which the readers may wish to refer for technical details omitted here.

2.1 Domain setup and forcings

All numerical simulations are in 2-D and solved using the dynamical core of the System for Atmospheric Modeling (Khairoutdinov and Randall, 2003). The simulations are subject to perturbations (in temperature and velocities) of a large-scale equatorial Kelvin wave (see Dinh et al., 2012, Sect. 3.2, for the mathematical details). The wavelength and period of the wave are respectively 6000 km and 6 d (see Dinh et al., 2012, Figs. 2 and 3). The model is integrated over two cycles of the Kelvin wave (12 d) with a time step of $\triangle t = 20$ s.

The horizontal domain is 6000 km, i.e. the wavelength of the Kelvin wave. Periodic boundary conditions are applied on the lateral edges of the domain. In the vertical, the model domain extends from $z = 15$ to 18 km. Non-reflective open boundary conditions (Bougeault, 1983; Klemp and Durran, 1983) are applied at the top and bottom of the domain. In the horizontal, the resolution is $\triangle x = 5$ km. In the vertical, $\triangle z$ varies from 5 m in the proximity of the cold-point tropopause (CPT, at $z = 17.3$ km) to 50 m at the top and bottom of the domain. The base-state (unperturbed) temperature profile $\widetilde{T}(z)$ is taken from a sounding typical for the tropics (see Dinh et al., 2012, Fig. 1).

2.2 Cloud processes

Ice nucleation is computed for homogeneous freezing (Koop et al., 2000). We assume a fixed background aerosol with a concentration of 100 cm^{-3} and a diameter of 0.5 µm. This is consistent with observed aerosol properties in the upper troposphere and lower stratosphere (Chen et al., 1998). Ice depositional growth and sublimation are solved using the bin scheme designed by Dinh and Durran (2012). The size distribution of ice crystals is resolved with 25 bins ranging from 0.5 to 50 µm in diameter. Fall speeds of ice crystals are computed following Böhm (1989).

In the most complete all-phys simulations, all microphysical processes, including ice nucleation, depositional growth and sublimation, and sedimentation, are explicitly resolved with the bin scheme. Additionally, we compute the radiative heating that results from absorption of radiation by ice crystals using the radiative transfer scheme described in Durran et al. (2009, Sect. 3a). The gas-phase radiative response

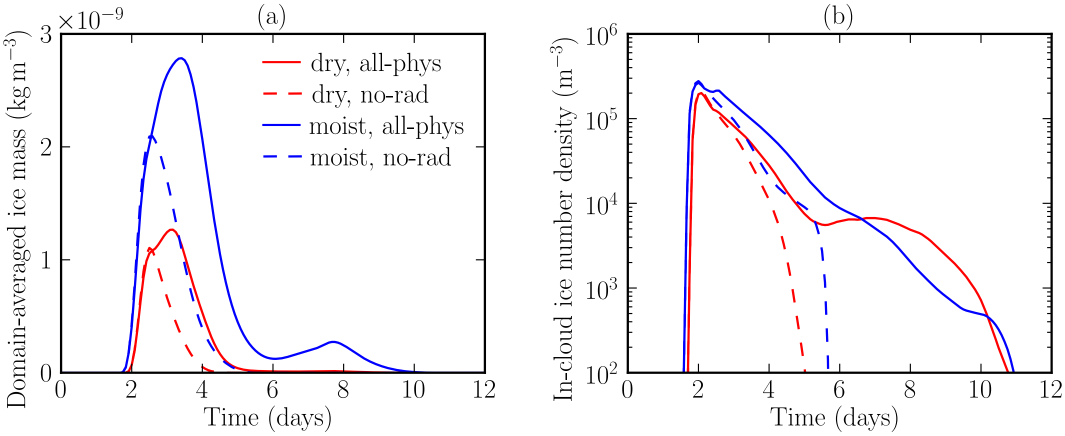

Figure 1. Evolution of **(a)** the domain-averaged ice mass and **(b)** the ice number density averaged over the cloudy area in the no-rad and all-phys simulations for both the dry and moist scenarios.

to cloud-induced temperature perturbations, T'_c, is modelled with Newtonian cooling, $Q_N = -\frac{T'_c}{\gamma}$. The radiative relaxation timescale γ is set to 20 d (see Hartmann et al., 2001, Fig. 1). As further discussed in Sect. 3.1, the cloud radiative heating induces (i) a cloud-scale circulation (itself a gravity wave signal) and (ii) small-scale convective cells at the cloud top, whose buoyancy forces generate small-scale gravity waves which propagate vertically outwards from the convective layer (see also Dinh et al., 2010). The all-phys simulations fully resolve the perturbations (in both temperature and velocities) of these gravity waves generated by the cloud radiative heating. The importance of gravity waves to the microphysical processes in TTL cirrus has also been suggested by Jensen and Pfister (2004) and Spichtinger and Krämer (2013).

In the no-rad simulations, the cloud radiative heating is (artificially) turned off. Hence the Kelvin wave perturbations determine all the thermodynamic conditions governing cloud formation and subsequent evolution.

In the inf-sed simulations, ice nucleation is computed as in the no-rad simulations. However, the microphysics for post-nucleation are drastically simplified by assuming instantaneous dehydration to the saturation vapour mixing ratio q_s upon nucleation. Specifically, at the time and location when/where the threshold for homogeneous ice nucleation (relative humidity with respect to ice $RH_i \approx 160\,\%$ in the TTL) is reached, water vapour in excess of saturation is immediately removed by ice particles sedimenting out of the domain at an infinite fall speed.

2.3 Initial conditions

The humidity profile is initialised with a background specific humidity of $q_v = 2.09 \times 10^{-6}\,\mathrm{kg\,kg^{-1}}$ ("moist" scenario) and $1.40 \times 10^{-6}\,\mathrm{kg\,kg^{-1}}$ ("dry" scenario). These values correspond respectively to $RH_i = 120$ and 80 % around $z = 17$ km. In both scenarios, the humidity is increased smoothly from the ambient values to $RH_i = 150\,\%$ in a region at the centre of the horizontal domain (between $x = 2700$ and 3300 km) and around the CPT. The 2-D profiles of the initial q_v and RH_i for the dry scenario are illustrated in Dinh et al. (2012, Fig. 4).

These initial conditions, in combination with the Kelvin wave forcings, produce thin cirrus clouds around the tropopause that are both similar to observations (see Dinh et al., 2012, for comparison between model simulations and observations) and confined within the model domain for the entire duration of simulation. In both scenarios the initial moisture profiles at the bottom of the domain ($z = 15$ km) are in general at the drier end of observed humidities. Nevertheless, for the moist scenario, our RH_i is similar to the in situ measurements reported by Jensen et al. (2005, Fig. 1)[1]. We have chosen these profiles deliberately to ensure that, in the no-rad and all-phys simulations, no particles sediment out of the domain, and hence the model domain captures the entire process of moisture redistribution.

Within the initially prescribed moist region near the CPT, the nucleation threshold ($RH_i \approx 160\,\%$) is reached when negative temperature perturbations of the Kelvin wave arrive at the centre of the domain (at $t = 1.75$ d). In the inf-sed simulations, q_v decreases immediately to the saturation vapour mixing ratio q_s within this region at this time. In the no-rad and all-phys simulations, as ice depositional growth takes place within the clouds, q_v remains close to q_s for most of the cloudy air. Hence, in the layer where the clouds form and ice crystals grow, the cloudy air contains more (less) water vapour than the subsaturated (supersaturated) environment in the dry (moist) scenario.

[1]Note that the comprehensive instrumentation evaluation by Fahey et al. (2014) suggests that measurement errors may have caused overestimation in the relative humidity reported in Jensen et al. (2005).

2.4 Trajectory computation

We calculate domain-filling air parcel trajectories, initialised on a grid of 5 km horizontally and 2.5 m vertically. Equal spacing in geometric space (rather than proportional to mass) was chosen because we will not quantify mass fluxes but instead fractions of the model domain that experience specific conditions (for example nucleation).

Trajectories of air parcels are computed using a Lagrangian parcel-tracking scheme written by Yamaguchi and Randall (2012). The scheme predicts the trajectories based on the iterative Euler–Heun method with spatially interpolated resolved-scale velocity. We use three iterations to compute the resolved-scale velocity at half time steps and a third-order Lagrange polynomial interpolation to interpolate the Eulerian grid-point values (of velocities and scalars) to the parcel locations. As water vapour and ice along the trajectories are computed from the interpolated Eulerian grid-point values, we automatically account for the exchange of ice between different air parcels due to ice sedimentation.

In the all-phys simulations, the trajectories follow the complex fluid motions which are the sum of the large-scale Kelvin wave velocities and smaller-scale radiatively induced velocities, while in the other simulations the trajectories follow the Kelvin wave motions only.

3 Results

3.1 Cloud evolution

The cloud evolution in the 2-D domain in the all-phys simulation for the dry scenario is illustrated in the Supplement[2] of Dinh et al. (2012). Here Fig. 1 shows the cloud evolution in the all-phys and no-rad simulations for both the dry and moist scenarios. The difference in the background moisture of 40 % between the dry and moist scenarios leads to a much larger part of the domain being at and above saturation in the moist scenario. This results in a considerably larger cloud area in the moist scenario, which largely accounts for a difference in the domain-averaged ice mass of about 250 % between the simulations for the two scenarios (Fig. 1a). As shown in Fig. 1b, the ice number density averaged within the cloud area (not over the entire domain) is also higher in the moist scenario. In the moist scenario, the nucleation threshold is reached (and nucleation begins) at a slightly earlier time during the Kelvin wave passage when the cooling rate is higher.

In addition, Fig. 1 shows that the cloud evolution is sensitive to the cloud radiatively induced perturbations. For both the dry and moist scenarios, the radiatively induced circulation leads to an extension of the cloud area that explains to some extent the larger domain-averaged ice mass in the all-phys compared with no-rad simulations. Furthermore, in both the dry and moist scenarios, the all-phys simulations retain a higher ice number density after the first nucleation bursts around day 2. The reasons for these differences between the all-phys and no-rad simulations are explained below.

[2]Downloadable at www.atmos-chem-phys.net/12/9799/2012/acp-12-9799-2012-supplement.zip

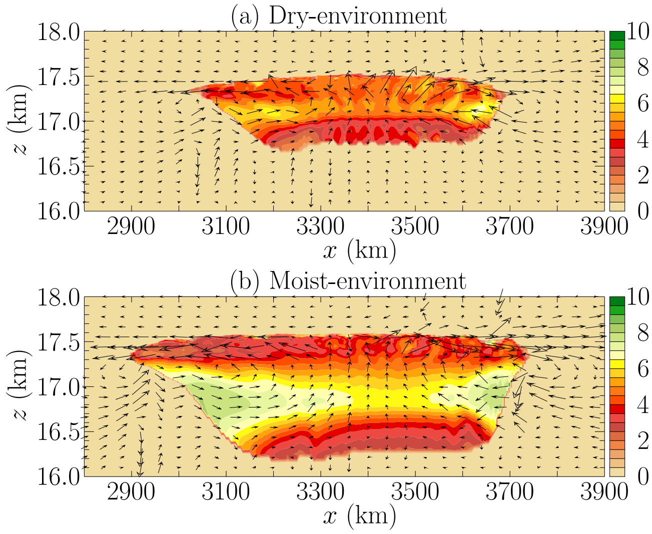

Figure 2. Mean crystal radius (µm) at $t = 3.5$ d in the all-phys simulations in **(a)** the dry scenario and **(b)** the moist scenario. Vectors show the radiatively induced motions.

Figure 2 shows the mean ice crystal radius at $t = 3.5$ d in the all-phys simulations for the dry (top panel) and moist (bottom panel) scenarios. Also shown are the wind vectors induced by the cloud radiative heating. The thermally induced cloud-scale circulation consists of ascent centred in the cloudy region which is surrounded and balanced by subsidence. Consistent with the conservation of mass, the vertical motions are accompanied by horizontal inflow in the lower half of the cloud layer and horizontal outflow in the upper half. For detailed theoretical and numerical descriptions of the dynamics induced by a stratiform mesoscale heat source, see Durran et al. (2009) and Dinh et al. (2010, 2012).

As described above, the radiative heating induces in-cloud updrafts. These counteract ice sedimentation and contribute to longer cloud lifetimes in the all-phys simulations compared with the no-rad simulations (see Fig. 1). Meanwhile, the radiatively induced horizontal motions widen the cloud top and narrow the cloud base. As the cloud deforms into trapezoidal shapes (Fig. 2), ice crystals fall into initially ice-free air at the (tilted) lateral sides of the cloud (and also at the cloud base). At the sides of the cloud in regions subject to horizontal inflow of environmental air, ice crystals grow to larger sizes in the moist scenario (where the ambient air is supersaturated) than in the dry scenario (where the ambient air is subsaturated).

In addition to inducing a cloud-scale circulation (as described above), the cloud radiative heating destabilises a thin

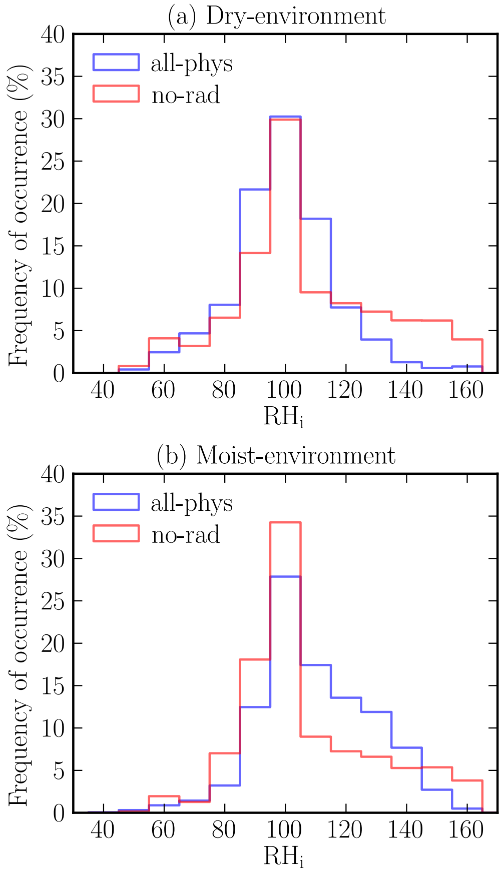

Figure 3. Frequency distribution of in-cloud relative humidities over the cloud lifetimes.

layer at the cloud top in the all-phys simulations. Soon after the first bursts of ice nucleation, small-scale convection develops and causes turbulent mixing and ice nucleation in the destabilised layer. Since the ice particle number density nucleated in the destabilised layer in the all-phys simulations is similar to that in the rest of the cloud, the in-cloud average ice number density (Fig. 1b) is similar in the all-phys and no-rad simulations between day 2 and 3, while the total ice mass (Fig. 1a) and the total number of particles (not shown) are larger in the all-phys simulations.

As shown in Fig. 3, the distribution of in-cloud relative humidities maximises at 100 %, i.e. the largest fraction of the cloudy air is maintained close to saturation throughout the cloud lifetimes. Larger departures from 100 % of in-cloud relative humidities occur where the ice number concentration is low, and/or where the temperature perturbations (due to the imposed Kelvin wave in all model simulations, and cloud-induced gravity waves in the all-phys simulations) are large, and/or where mixing with the environment occurs. In the no-rad simulations, initially cloud-free air becomes cloudy only at the cloud base (due to ice sedimentation). In the all-phys simulations, both the cloud circulation and the convective turbulence at the cloud top enhance mixing of environmental air into the cloud. As a consequence, the frequency of in-cloud supersaturation in the all-phys simulation is lower than in the no-rad simulation for the dry scenario (where the ambient air is subsaturated). Conversely, the frequency of in-cloud supersaturation in the all-phys simulation is higher than in the no-rad simulation for the moist scenario (where the ambient air is supersaturated).

3.2 Cloud-induced redistribution of moisture

Figure 4 shows the changes in the water vapour mixing ratio profiles in all model simulations. The notations $[q_v^i]$, $[q_v^f]$, and $[\triangle q_v]$ respectively denote the horizontal-domain averages of the initial and final q_v profiles and of the changes in q_v profiles (final minus initial).

Recall that the model domain has been designed to capture all the moisture redistribution in the all-phys and no-rad simulations. For the inf-sed simulations, ice crystals are removed instantaneously without sublimating at lower levels, and the domain-averaged water vapour is not conserved. The lack of hydration at lower levels in the inf-sed simulations is thus not surprising per se. Rather, of interest here is the question of to what extent the strongly simplified inf-sed calculation captures the dehydration induced by the cloud.

In the no-rad simulations (for both the dry and moist scenarios), dehydration ($[\triangle q_v](z) < 0$) occurs within the initially prescribed moist region in the centre of the domain. The magnitude of dehydration in the dehydrated layer increases with the initial available moisture (larger in the moist scenario). Ice nucleation and depositional growth, followed by ice sedimentation and sublimation consistently lead to downward transport of water vapour in the no-rad simulations. As a consequence of ice sedimentation, the dehydrated layer lies above the hydrated layer.

The vertical integral of $[\triangle q_v]$ over the dehydrated layer (i.e. excluding the areas that have been moistened) is more negative in the no-rad simulations than in the inf-sed simulations. In the inf-sed simulations, dehydration starts and stops instantaneously when the nucleation threshold is reached; this occurs before the arrival of the minimum temperature of the Kelvin wave passage. In the no-rad simulations, additional dehydration is obtained due to growth of newly formed ice crystals as temperature continues to decrease after nucleation. Furthermore, in the no-rad simulations, dehydration occurs both inside and below the layer in which ice nucleation occurs. Below the region of ice nucleation, dehydration occurs as ice crystals fall into initially supersaturated but ice-free air and grow from the available moisture.

Figure 4 shows that the effect of the cloud radiatively induced perturbations is sensitive to the initial moisture. For the dry scenario, in the all-phys simulation, a thin layer between $z = 16.9$ and 17.1 km becomes dehydrated (Fig. 4a and b), but not all of the water removed from the dehydrated layer is transported downward. In fact, a region above the dehydrated layer has been moistened (in which $[\triangle q_v] > 0$) and the inte-

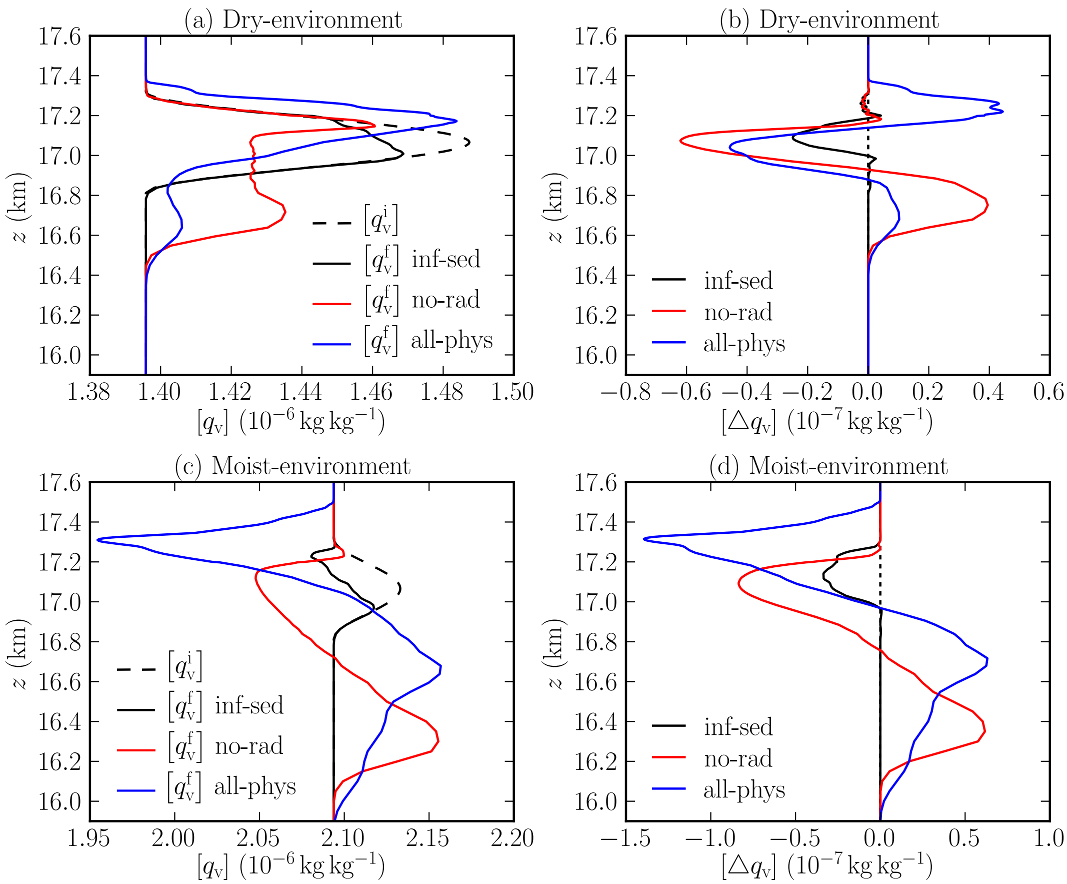

Figure 4. The horizontal-domain average of the initial and final water vapour mixing ratio q_v (left column), and changes in q_v (right column) in the dry (top row) and moist (bottom row) scenarios.

gral of $[\triangle q_v]$ in this hydrated layer is 69 % of the mass of water vapour loss from the dehydrated layer. In other words, 69 % of the water from the dehydrated layer has been transported upward and the remaining 31 % has been transported downward by ice sedimentation. Thus, the direction of the net water vapour flux is upward in the all-phys simulation in the dry scenario. On the other hand, for the moist scenario (Fig. 4c and d), the direction of the net water vapour flux is downward, and the mass of water vapour removed from the dehydrated layer is enhanced (by about 45 %) in the all-phys simulation compared with the no-rad simulation.

For both the dry and moist scenarios, the radiatively induced circulation advects the cloudy air upwards. The direction of the water vapour flux associated with this upward advection of the cloudy air is sensitive to the vapour content of the cloudy air relative to the environment. When the cloud is surrounded by drier environmental air (in the dry scenario), upward advection of the cloudy air (which contains more water vapour than the environmental air) results in an upward flux of water vapour. Conversely, when the cloud is surrounded by moister air (in the moist scenario), upward advection of the cloudy air (which is close to saturation while the environment is weakly supersaturated) results in a downward flux of water vapour.

To separate the advective tendencies from the impacts of microphysical processes, we compute the accumulative mass of water associated with ice-to-vapour exchange during the model integration (Fig. 5). The exchange of water between the vapour and ice phases is recorded at the time and location when/where (de)hydration occurs throughout the model integration. With the advective tendencies excluded, Fig. 5 shows that microphysical processes consistently lead to dehydration in the upper half of the cloud layer (in contrast to Fig. 4b, where the advective tendencies result in hydration above 17.1 km in the all-phys simulation for the dry scenario). A comparison between the no-rad and all-phys profiles in Fig. 5 shows that the radiatively induced perturbations enhance the impact of cloud microphysics in redistributing the moisture profiles. This holds in terms of both the magnitude and the thickness of the (de)hydrated layers.

3.3 Lagrangian analysis

The Lagrangian analysis is based on the domain-filling trajectories as described in Sect. 2.4. The trajectories begin at

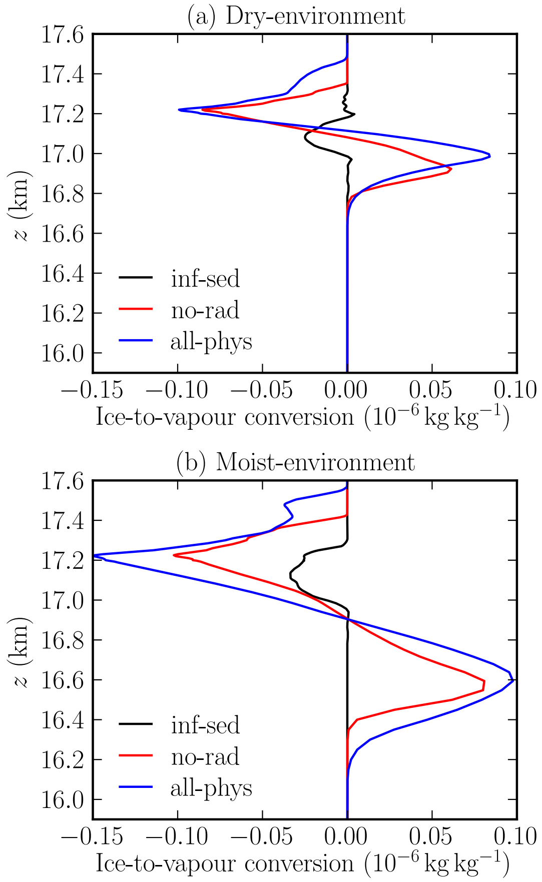

Figure 5. The profiles of accumulative mass exchange from ice to vapour over the model integration in **(a)** the dry scenario and **(b)** the moist scenario.

the same initial grid points in the different model calculations, but they evolve differently in the all-phys simulations and those with reduced physics. The trajectories are the same in the no-rad and inf-sed simulations where they follow the Kelvin wave flow.

Parcels travelling along the trajectories are deemed to have dehydrated (by the formation and growth of ice crystals) or hydrated (by the sublimation of ice crystals falling into the parcels) if the magnitude of the specific humidity change (δq_{v}, final minus initial specific humidity of the air parcels) exceeds $\epsilon = 5 \times 10^{-8}$ kg kg^{-1}. In the absence of mixing, only the source and sink terms associated with microphysical processes (non-advective tendencies) contribute to δq_{v}. However, diffusion and numerical errors (associated with interpolation in the Lagrangian parcel calculation; see Sect. 2.4) inevitably require that we allow for some margin $\epsilon > 0$ (as given above). The "dehydration" and "hydration" criteria are defined as respectively $\delta q_{\mathrm{v}} < -\epsilon$ and $\delta q_{\mathrm{v}} > \epsilon$. Using the same margin ϵ, the "cloud" criterion is defined as $q_{\mathrm{i}} > \epsilon$ at any time during the model integration, where q_{i} is the ice mixing ratio along the parcel trajectories. The cloud criterion

Table 1. The number of cloudy air parcels N_{c}, and the fraction of parcels within the set N_{c} that are dehydrated and hydrated in all model simulations.

Scenario	Case	$\frac{N^-}{N_{\mathrm{c}}}$	$\frac{N^+}{N_{\mathrm{c}}}$
Dry	all-phys	0.43	0.53
$N_{\mathrm{c}} = 2.4 \times 10^4$	no-rad	0.31	0.42
	inf-sed	0.26	0
Moist	all-phys	0.47	0.37
$N_{\mathrm{c}} = 8.2 \times 10^4$	no-rad	0.24	0.27
	inf-sed	0.14	0

identifies the parcels that pass by the cloud at some point during the model integration.

Figure 6 and the supplemental animations show representative trajectories of (de)hydrated air parcels in the no-rad and all-phys simulations for both the dry and moist scenarios. The animations show that trajectories of air parcels are significantly modified by the motions induced by the cloud radiative heating. In addition, because of ice sedimentation, dehydrated air parcels tend to be located above hydrated parcels. In the moist scenario, there is a near-saturated layer separating dehydrated air (above) from hydrated air (below). Ice crystals fall through this layer without significant growth or sublimation. Air parcels that pass through the cloud in this near-saturated layer satisfy the cloud criterion but do not dehydrate or hydrate significantly. This illustrates that the set of dehydrated and hydrated air parcels is a subset of the set of cloudy air parcels.

Using the above definitions for cloudy, dehydrated, and hydrated air parcels, below we compute (i) the fraction of the cloud that experiences nucleation and (ii) the changes in the specific humidity of cloudy air parcels over the model integration.

3.3.1 Nucleation

The fraction of the cloud that experiences nucleation is calculated separately for the dry and moist scenarios. In the inf-sed simulations, there is virtually no cloud because all ice crystals fall out instantaneously. Thus the cloudy air is defined based on the no-rad and all-phys simulations. Let N_{c} denote the number of air parcels that satisfy the cloud criterion ($q_{\mathrm{i}} > \epsilon$ at any time during the model integration) in at least one of the no-rad or all-phys simulations. This comprises the set of cloudy air parcels.

In the inf-sed case, all air parcels that experience nucleation dehydrate, and there is neither dehydration nor hydration for air parcels that do not experience nucleation. For each moisture scenario, all thermodynamic conditions are identical in all three model simulations up to the nucleation time. Hence the set of air parcels that experience nucleation in the inf-sed case is the same as those that experience nucleation in the no-rad case. In the all-phys case, additional, sub-

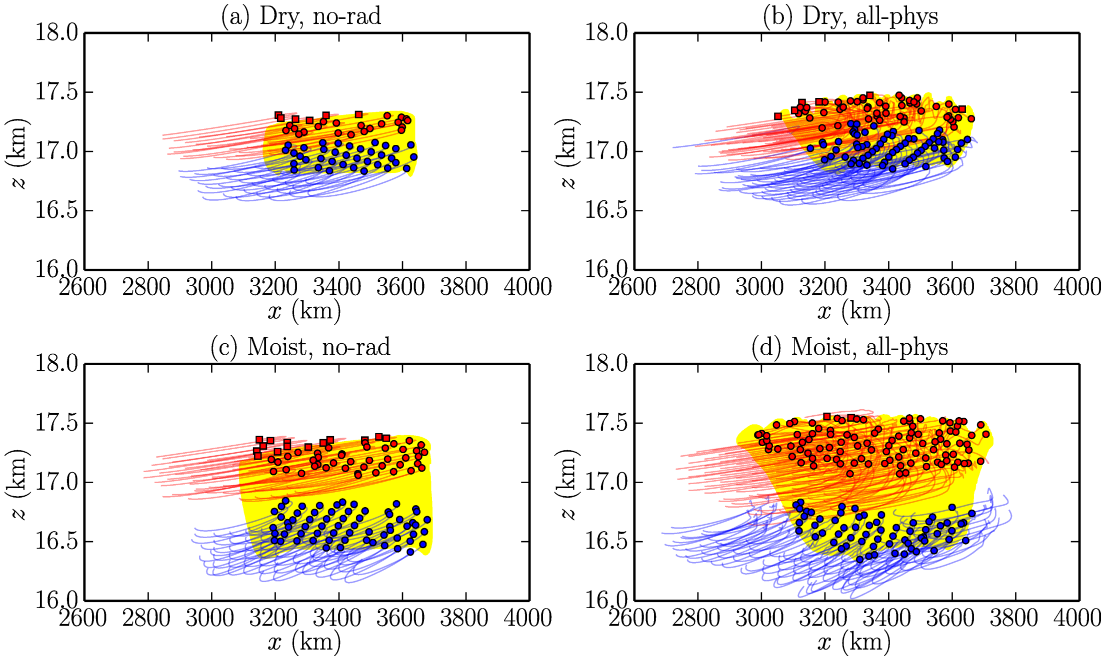

Figure 6. The cloud at $t = 3.5$ d (yellow-shaded region) and representative air parcel trajectories from $t = 0$ to 3.5 d in the no-rad (left column) and all-phys (right column) simulations for the dry (top row) and moist (bottom row) scenarios. Trajectories of dehydrated and hydrated air parcels are shown in red and blue respectively. The locations of the parcels at 3.5 d are marked with circles if the parcels are inside the cloudy region, and with squares if the parcels passed through the cloud at earlier times and are in cloud-free air at 3.5 d. Some parcels (whose locations at 3.5 d are not indicated by squares or circles) have not entered the cloud (but will do so after 3.5 d).

sequent ice nucleation takes place in the destabilised layer at the cloud top due to turbulent mixing (as explained previously in Sect. 3.1).

Let $N^-_{\text{all-phys}}$ and $N^+_{\text{all-phys}}$ denote the number of (de)hydrated air parcels (satisfying the (de)hydrated criteria) in the all-phys case. The subscript is replaced by "no-rad" and "inf-sed" to refer to the two simplified model experiments. The fraction of the cloud that experiences nucleation as a direct response to the imposed Kelvin wave perturbations (no cloud radiative–dynamical feedbacks) is given by the fraction $N^-_{\text{inf-sed}}/N_{\text{c}}$, which is 0.26 and 0.14 in the dry and moist scenarios respectively (see Table 1). In other words, only 26 % (14 %) of the cloud experiences nucleation as a direct response to the imposed forcings in the dry (moist) scenario.

Furthermore, as also shown in Table 1, the inf-sed calculation underestimates dehydration compared to both the no-rad and all-phys calculations. In fact, $N^-_{\text{inf-sed}}$ is 84 % (58 %) of $N^-_{\text{no-rad}}$ in the dry (moist) scenario. In other words, 16 % (42 %) of dehydration in the no-rad simulation occurs outside of the nucleation region in the dry (moist) scenario. Dehydration occurs below the nucleation region as ice crystals fall into initially ice-free air that is supersaturated but not sufficiently moist to allow ice nucleation. The error in dehydration is even larger when the inf-sed case is compared with the all-phys case: $N^-_{\text{inf-sed}}$ is 60 % (30 %) of $N^-_{\text{all-phys}}$ in the dry (moist) scenario.

The notable conclusion is that most air parcels that constitute the cloud never experience nucleation (see Table 1). Rather, post-nucleation processes (ice growth, sedimentation, and sublimation) account for most of the "cloud." Furthermore, nucleation in the inf-sed calculation (a direct response to the imposed forcings neglecting most cloud physics) not only misses the hydration but also considerably underestimates the dehydrated area of the cloud.

3.3.2 Changes in specific humidity of cloudy air parcels

Figure 7 shows the histograms of δq_{v} of cloudy air parcels for all model simulations evaluated separately for the dry (top panel) and moist (bottom panel) scenarios. For each moisture scenario, the total number of counts over all δq_{v} bins in each experiment (all-phys, no-rad or inf-sed) is equal to N_{c} (defined in Sect. 3.3.1). The figure shows that the distribution of δq_{v} is sensitive to the initial conditions (dry versus moist), as described below.

For the dry scenario, the all-phys simulation gives a bimodal distribution (with peaks at large dehydration and hydration). The no-rad simulation captures the key features of this distribution, but has a third mode centred at zero. By construction, the inf-sed simulation has only trajectories that either dehydrate or are never in the cloud field. Of interest is

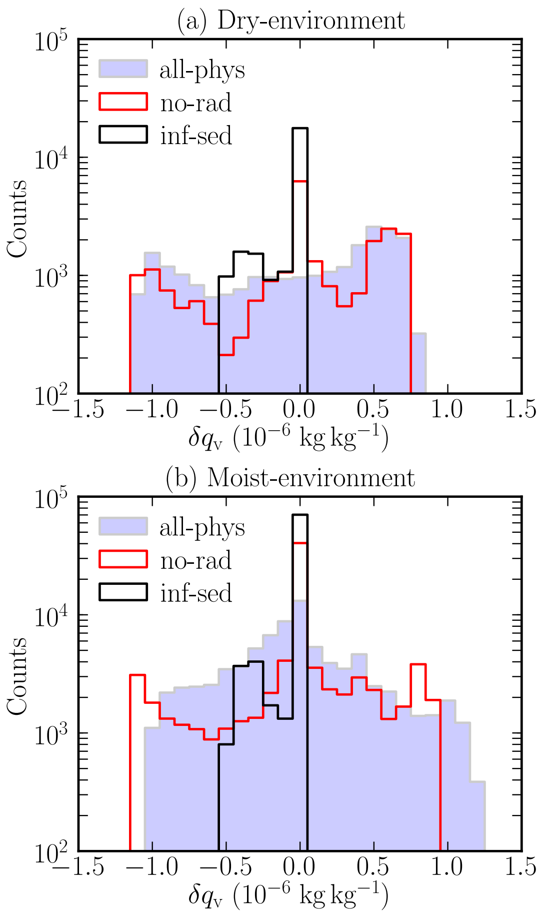

Figure 7. Histograms (in log scale) of changes in specific humidity over the integration (final minus initial) of all cloudy air parcels (for which $q_i > 5 \times 10^{-8}$ kg kg^{-1} in at least one of the all-phys or no-rad simulations).

that in the inf-sed case the maximum and average water loss are smaller than in the other two cases, a point we will return to below.

For the moist scenario, the distribution function of the all-phys simulation is concentrated at small $|\delta q_v|$ values, in contrast to the bimodality at large (de)hydration values in the dry scenario (compare the blue-shaded distributions in Fig. 7a and Fig. 7b). This difference between the dry and moist scenarios arises from the difference in the initial moisture. In the layer below the region where the cloud forms, temperature increases and hence RH_i decreases with decreasing height. Ice crystals fall through the layer where RH_i transitions from above 100 % to below 100 % (i.e. where the air is near saturation) without significant growth or sublimation. The central peak of the distribution at small $|\delta q_v|$ values in the all-phys simulation for the moist scenario (Fig. 7b) is associated with a large number of air parcels passing through this near-saturated layer (which has a noticeable depth in the moist scenario; see Fig. 6) without experiencing dehydration or hydration.

The left panels in Fig. 8 compare the changes in specific humidity of cloudy air parcels in the inf-sed case versus the all-phys case for the dry (top panel) and moist (bottom panel) scenarios. The joint histograms (Fig. 8a and c) show a large number of parcels for which the specific humidity is essentially unchanged in the inf-sed case, but significant dehydration or hydration occurs in the all-phys case. In addition, for dehydrated air parcels, δq_v is more negative in the all-phys case than in the inf-sed case for both the dry and moist scenarios (the data for $\delta q_v < 0$ lie above the one-to-one line in Fig. 8a and c). In other words, dehydrated parcels dehydrate more in the all-phys simulations. In the inf-sed simulations, the immediate fallout of ice crystals limits dehydration to the saturation mixing ratio q_s at the nucleation time. Subsequently, temperature never drops sufficiently low to bring the relative humidity above the nucleation threshold again. In the all-phys simulations, dehydration continues after nucleation due to depositional growth of ice crystals, and dehydration up to q_s at the minimum temperature of the Kelvin wave passage can be obtained.

The right panels in Fig. 8 show the joint histograms of δq_v in the no-rad case versus the all-phys case for the dry (top panel) and moist (bottom panel) scenarios. For the dry scenario (Fig. 8b), the bulk of air parcels in the two simulations experience relatively similar changes in specific humidity, namely either a dehydration of about -1.0×10^{-6} kg kg^{-1} or a hydration of about $+0.5 \times 10^{-6}$ kg kg^{-1}. The remainder of the joint histogram is dominated by parcels that are either dehydrated or hydrated in the all-phys case but for which $|\delta q_v| < \epsilon$ in the no-rad case. For the moist scenario, the joint histogram (Fig. 8d) is dominated by a large number of hydrated parcels in the all-phys case for which there are no significant changes in specific humidity in the no-rad case. In the all-phys simulation, many air parcels become hydrated as ice crystals fall into the initially ice-free, moist air at the tilted lateral sides of the cloud (see Fig. 2b). In addition, there is a clear deviation of the joint histogram in Fig. 8d from the one-to-one line.

In summary, the inf-sed calculation does not capture the presence of hydrated air parcels. Furthermore, it underestimates the magnitude of dehydration for dehydrated air parcels (see Fig. 8, left column). In comparison, the no-rad calculation (Fig. 8, right column) is much closer to the baseline vapour distribution of the cloudy air parcels given by the all-phys calculation. For the dry scenario, the key features of the distribution function of δq_v with peaks at large (de)hydration values are well represented by the no-rad calculation (Fig. 8b). However, for the moist scenario, the distribution of δq_v deviates significantly between the no-rad and all-phys simulations (Fig. 8d). Furthermore, for both the dry and moist scenarios, there are a large number of air parcels that experience (de)hydration in the all-phys simulations but almost no change in specific humidity in the no-rad simulations.

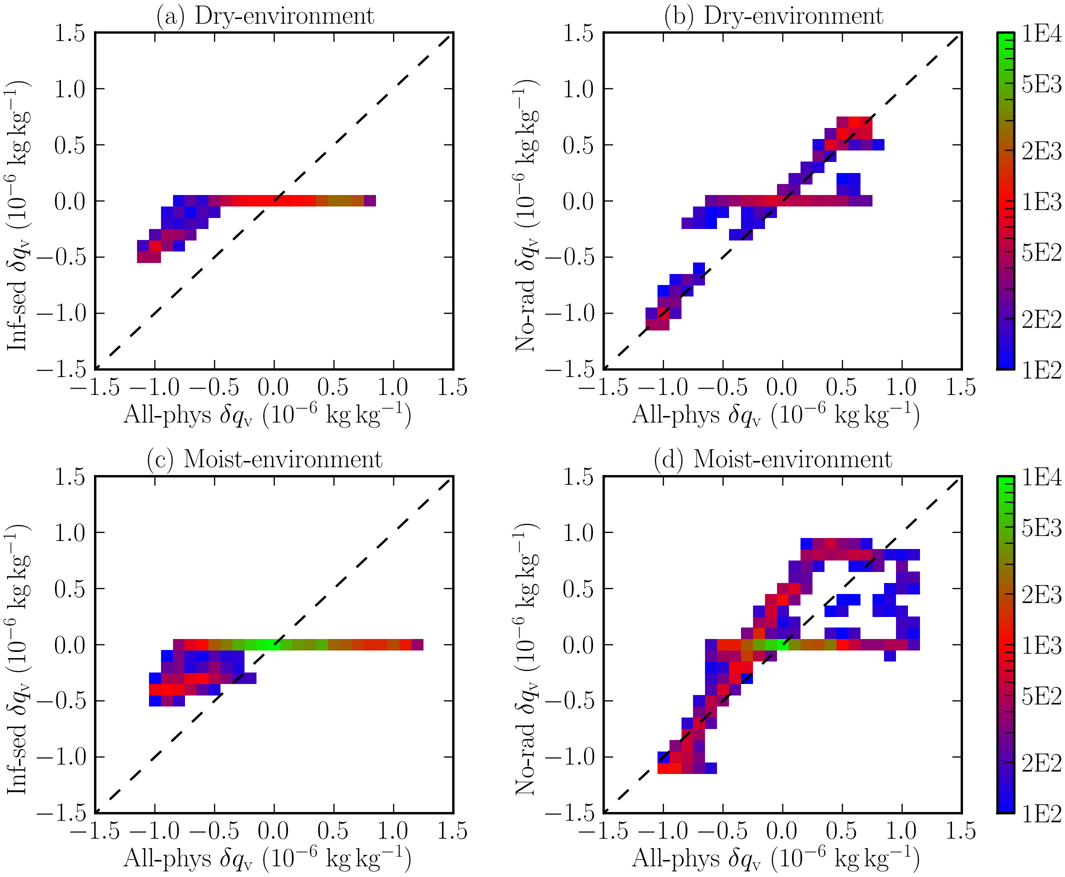

Figure 8. Changes in specific humidity of the cloudy air parcels in the inf-sed simulations versus the all-phys simulations (left column) and in the no-rad simulations versus the all-phys simulations (right column) for the dry (top row) and moist (bottom row) scenarios. The baseline water vapour distributions (abscissae in all four panels) are taken from the all-phys simulations. The dashed line shows the one-to-one slope. The colour bar shows the number of air parcel counts.

4 Conclusions

Numerical simulations of cirrus clouds in the tropical tropopause layer (TTL) have been carried out. The redistribution of moisture following cloud occurrences in the simulations is computed from the changes in water vapour over the domain of simulation (Eulerian perspective) and as following air parcels (Lagrangian perspective).

Both microphysical and dynamical processes are important contributors to the net cloud-induced redistribution of water vapour in the domain. Microphysical processes (ice nucleation and growth, followed by ice sedimentation and sublimation) always lead to downward transport of water vapour. On the other hand, the direction of the water vapour flux induced by the cloud circulation depends on the moisture content of the cloudy air relative to the environment. The radiative heating induces ascent in the cloudy area and hence upward advection of the cloudy air. When the cloudy air contains more water vapour than the surrounding environment (typically when the environmental air is subsaturated), upward advection of the cloudy air results in an upward flux of water vapour. Conversely, when the cloud contains less water vapour than the environment (typically when the environmental air is weakly supersaturated), upward advection of the cloudy air results in a downward flux of water vapour.

Regardless of the direction of the net water vapour flux in the Eulerian domain, air parcels that pass through the cloud top tend to lose water vapour (become dehydrated), and air parcels that pass through the cloud base tend to gain water vapour (become hydrated). Unless the bases of the clouds reach below the TTL, the hydrated air parcels remain in the TTL after the life cycles of the clouds. A complete removal of water vapour from the TTL may occur via a sequence of thin cirrus clouds each of which results in a limited downward displacement of hydrated air relative to dehydrated air. Because the hydrated air parcels may remain in the TTL for some time, observations of hydrated parcels despite the absence of convection (such as those reported by Inai et al., 2013) are expected wherever TTL cirrus have redistributed moisture.

Our numerical experiments show that the cloud evolution, as well as the degree and spatial extent to which a cloud modifies the water vapour profile, is very sensitive to the surrounding moisture. This sensitivity to the environmental moisture increases when the dynamical perturbations induced by the cloud radiative heating are considered in the model. Mixing between the cloud and the environment (through which initially cloud-free air becomes cloudy, and vice versa) are enhanced at the cloud top due to the radiatively induced convective turbulence, and at the lateral sides of the cloud due to the vertical shear of the radiatively induced horizontal motions. The numerical results show that both the spatial extent and the magnitude of the cloud-induced redistribution of moisture are underestimated when the radiative–dynamical feedbacks are neglected.

We have also carried out numerical experiments in which cloud processes are drastically simplified by assuming instantaneous dehydration to the saturation vapour mixing ratio whenever the homogeneous ice nucleation threshold is reached. That is, upon nucleation, ice crystals take up all moisture in excess of saturation and immediately sediment out of the domain (at an infinite fall speed). This assumption of instantaneous dehydration is sometimes used by simplified and/or large-scale models to compute dehydration of the air in the TTL while avoiding most complications associated with detailed cloud physics. These simplified model runs not only erroneously fail to capture the regions that have been moistened but also underestimate both the dehydrated area and the magnitude of dehydration within the dehydrated area. These conclusions have been obtained for homogeneous nucleation, and we expect the results to change quantitatively for heterogeneous nucleation (for which the nucleation threshold is lower).

The simulations have illustrated how the moisture redistribution induced by TTL cirrus depends on the (de)hydration process associated with ice sedimentation, cloud radiative–dynamical feedbacks, and mixing between the cloudy air and the environment. These processes are expected to affect how clouds modify the water vapour distribution not only for TTL cirrus but also for other types of clouds in general. These high-resolution simulations demonstrate that the complexity of the cloud-induced moisture redistribution needs to be considered especially for interpretations of high-resolution measurements of water vapour.

The Supplement related to this article is available online at doi:10.5194/acp-14-12225-2014-supplement.

Acknowledgements. We are grateful to Marat Khairoutdinov for sharing the System for Atmospheric Modeling, and Tak Yamaguchi for sharing the Lagrangian parcel-tracking model. We also would like to thank two anonymous reviewers, whose comments helped improve the manuscript. This research was supported by the NOAA Climate and Global Change Postdoctoral Fellowship Program, DOE grant SC0006841, and NSF grant AGS-1417659.

Edited by: T. Garrett

References

Boehm, M. T. and Verlinde, J.: Stratospheric influence on upper tropospheric tropical cirrus, Geophys. Res. Lett., 27, 3209–3212, doi:10.1029/2000GL011678, 2000.

Böhm, H. P.: A general equation for the terminal fall speed of solid hydrometeors, J. Atmos. Sci., 46, 2419–2427, doi:10.1175/1520-0469(1989)046<2419:AGEFTT>2.0.CO;2, 1989.

Bougeault, P.: A non-reflective upper boundary condition for limited-height hydrostatic models, Mon. Weather Rev., 111, 420–429, doi:10.1175/1520-0493(1983)111<0420:ANRUBC>2.0.CO;2, 1983.

Brewer, A. W.: Evidence for a world circulation provided by the measurements of helium and water vapour distribution in the stratosphere, Q. J. Roy. Meteor. Soc., 75, 351–363, doi:10.1002/qj.49707532603, 1949.

Chen, Y., Kreidenweis, S. M., McInnes, L. M., Rogers, D. C., and DeMott, P. J.: Single particle analyses of ice nucleating aerosols in the upper troposphere and lower stratosphere, Geophys. Res. Lett., 25, 1391–1394, doi:10.1029/97GL03261, 1998.

Dinh, T. and Durran, D. R.: A hybrid bin scheme to solve the condensation/evaporation equation using a cubic distribution function, Atmos. Chem. Phys., 12, 1003–1011, doi:10.5194/acp-12-1003-2012, 2012.

Dinh, T. and Fueglistaler, S.: Cirrus, Transport, and Mixing in the Tropical Upper Troposphere, J. Atmos. Sci., 71, 1339–1352, doi:10.1175/JAS-D-13-0147.1, 2014a.

Dinh, T. and Fueglistaler, S.: Microphysical, radiative and dynamical impacts of thin cirrus clouds on humidity in the tropical tropopause layer and stratosphere, Geophys. Res. Lett., 41, 6949–6955, doi:10.1002/2014GL061289, 2014b.

Dinh, T., Durran, D. R., and Ackerman, T.: Maintenance of tropical tropopause layer cirrus, J. Geophys. Res., 115, D02104, doi:10.1029/2009JD012735, 2010.

Dinh, T., Durran, D. R., and Ackerman, T.: Cirrus and water vapor transport in the tropical tropopause layer – Part 1: A specific case modeling study, Atmos. Chem. Phys., 12, 9799–9815, doi:10.5194/acp-12-9799-2012, 2012.

Durran, D. R., Dinh, T., Ammerman, M., and Ackerman, T.: The mesoscale dynamics of thin tropical tropopause cirrus, J. Atmos. Sci., 66, 2859–2873, doi:10.1175/2009JAS3046.1, 2009.

Fahey, D. W., Gao, R.-S., Möhler, O., Saathoff, H., Schiller, C., Ebert, V., Krämer, M., Peter, T., Amarouche, N., Avallone, L. M., Bauer, R., Bozóki, Z., Christensen, L. E., Davis, S. M., Durry, G., Dyroff, C., Herman, R. L., Hunsmann, S., Khaykin, S. M., Mackrodt, P., Meyer, J., Smith, J. B., Spelten, N., Troy, R. F., Vömel, H., Wagner, S., and Wienhold, F. G.: The AquaVIT-1 intercomparison of atmospheric water vapor measurement techniques, Atmos. Meas. Tech., 7, 3177–3213, doi:10.5194/amt-7-3177-2014, 2014.

Forster, P. M. d. F. and Shine, K. P.: Assessing the climate impact of trends in stratospheric water vapor, Geophys. Res. Lett., 29, 1086, doi:10.1029/2001GL013909, 2002.

Fueglistaler, S. and Haynes, P. H.: Control of interannual and longer-term variability of stratospheric water vapor, J. Geophys. Res., 110, D24 108, doi:10.1029/2005JD006019, 2005.

Fueglistaler, S., Bonazzola, M., Haynes, P. H., and Peter, T.: Stratospheric water vapor predicted from the Lagrangian temperature history of air entering the stratosphere in the tropics, J. Geophys. Res., 110, D08 107, doi:10.1029/2004JD005516, 2005.

Fueglistaler, S., Dessler, A. E., Dunkerton, T. J., Folkins, I., Fu, Q., and Mote, P. W.: Tropical tropopause layer, Rev. Geophys., 47, RG1004, doi:10.1029/2008RG000267, 2009.

Fueglistaler, S., Liu, Y. S., Flannaghan, T. J., Haynes, P. H., Dee, D. P., Read, W. J., Remsberg, E. E., Thomason, L. W., Hurst, D. F., Lanzante, J. R., and Bernath, P. F.: The relation between atmospheric humidity and temperature trends for stratospheric water, J. Geophys. Res., 118, 1052–1074, doi:10.1002/jgrd.50157, 2013.

Fujiwara, M., Iwasaki, S., Shimizu, A., Inai, Y., Shiotani, M., Hasebe, F., Matsui, I., Sugimoto, N., Okamoto, H., Nishi, N., Hamada, A., Sakazaki, T., and Yoneyama, K.: Cirrus observations in the tropical tropopause layer over the western Pacific, J. Geophys. Res., 114, D09304, doi:10.1029/2008JD011040, 2009.

Gettelman, A., Randel, W. J., Wu, F., and Massie, S. T.: Transport of water vapor in the tropical tropopause layer, Geophys. Res. Lett., 29, 9-1–9-4 doi:10.1029/2001GL013818, 2002.

Hartmann, D. L., Holton, J. R., and Fu, Q.: The heat balance of the tropical tropopause, cirrus, and stratospheric dehydration, Geophys. Res. Lett., 28, 1969–1972, doi:10.1029/2000GL012833, 2001.

Hoskins, B. J.: Towards a PV-θ view of the general circulation, Tellus A, 43, 27–35, doi:10.1034/j.1600-0870.1991.t01-3-00005.x, 1991.

Immler, F., Krüger, K., Fujiwara, M., Verver, G., Rex, M., and Schrems, O.: Correlation between equatorial Kelvin waves and the occurrence of extremely thin ice clouds at the tropical tropopause, Atmos. Chem. Phys., 8, 4019–4026, doi:10.5194/acp-8-4019-2008, 2008.

Inai, Y., Hasebe, F., Fujiwara, M., Shiotani, M., Nishi, N., Ogino, S.-Y., Vömel, H., Iwasaki, S., and Shibata, T.: Dehydration in the tropical tropopause layer estimated from the water vapor match, Atmos. Chem. Phys., 13, 8623–8642, doi:10.5194/acp-13-8623-2013, 2013.

James, R., Bonazzola, M., Legras, B., Surbled, K., and Fueglistaler, S.: Water vapor transport and dehydration above convective outflow during Asian monsoon, Geophys. Res. Lett., 35, L20810, doi:10.1029/2008GL035441, 2008.

Jensen, E. and Pfister, L.: Transport and freeze-drying in the tropical tropopause layer, J. Geophys. Res., 109, D02207, doi:10.1029/2003JD004022, 2004.

Jensen, E. J., Smith, J. B., Pfister, L., Pittman, J. V., Weinstock, E. M., Sayres, D. S., Herman, R. L., Troy, R. F., Rosenlof, K., Thompson, T. L., Fridlind, A. M., Hudson, P. K., Cziczo, D. J., Heymsfield, A. J., Schmitt, C., and Wilson, J. C.: Ice supersaturations exceeding 100% at the cold tropical tropopause: implications for cirrus formation and dehydration, Atmos. Chem. Phys., 5, 851–862, doi:10.5194/acp-5-851-2005, 2005.

Khairoutdinov, M. F. and Randall, D. A.: Cloud resolving modeling of the ARM summer 1997 IOP: Model formulation, results, uncertainties, and sensitivities, J. Atmos. Sci., 60, 607–625, doi:10.1175/1520-0469(2003)060<0607:CRMOTA>2.0.CO;2, 2003.

Klemp, J. B. and Durran, D. R.: An upper boundary condition permitting internal gravity wave radiation in numerical mesoscale models, Mon. Weather Rev., 111, 430–444, doi:10.1175/1520-0493(1983)111<0430:AUBCPI>2.0.CO;2, 1983.

Koop, T., Luo, B., Tsias, A., and Peter, T.: Water activity as the determinant for homogeneous ice nucleation in aqueous solutions, Nature, 406, 611–614, doi:10.1038/35020537, 2000.

Liu, Y. S., Fueglistaler, S., and Haynes, P. H.: Advection-condensation paradigm for stratospheric water vapor, J. Geophys. Res, 115, D24307, doi:10.1029/2010JD014352, 2010.

Mace, G. G., Zhang, Q., Vaughan, M., Marchand, R., Stephens, G., Trepte, C., and Winker, D.: A description of hydrometeor layer occurrence statistics derived from the first year of merged Cloudsat and CALIPSO data, J. Geophys. Res., 114, D00A26, doi:10.1029/2007JD009755, 2009.

Massie, S., Gettelman, A., Randel, W., and Baumgardner, D.: Distribution of tropical cirrus in relation to convection, J. Geophys. Res., 107, 4591, doi:10.1029/2001JD001293, 2002.

Randel, W. J. and Jensen, E. J.: Physical processes in the tropical tropopause layer and their roles in a changing climate, Nat. Geosci., 6, 169–176, doi:10.1038/ngeo1733, 2013.

Ren, C., MacKenzie, A. R., Schiller, C., Shur, G., and Yushkov, V.: Diagnosis of processes controlling water vapour in the tropical tropopause layer by a Lagrangian cirrus model, Atmos. Chem. Phys., 7, 5401–5413, doi:10.5194/acp-7-5401-2007, 2007.

Schmidt, C. T. and Garrett, T. J.: A Simple Framework for the Dynamic Response of Cirrus Clouds to Local Diabatic Radiative Heating, J. Atmos. Sci., 70, 1409–1422, doi:10.1175/JAS-D-12-056.1, 2013.

Solomon, S., Garcia, R. R., Rowland, S. F., and Wuebbles, D. J.: On the depletion of Antarctic ozone, Nature, 321, 755–758, doi:10.1038/321755a0, 1986.

Solomon, S., Rosenlof, K. H., Portmann, R. W., Daniel, J. S., Davis, S. M., Sanford, T. J., and Plattner, G.-K.: Contributions of stratospheric water vapor to decadal changes in the rate of global warming, Science, 327, 1219–1223, doi:10.1126/science.1182488, 2010.

Spichtinger, P. and Krämer, M.: Tropical tropopause ice clouds: a dynamic approach to the mystery of low crystal numbers, Atmos. Chem. Phys., 13, 9801–9818, doi:10.5194/acp-13-9801-2013, 2013.

Virts, K. S., Wallace, J. M., Fu, Q., and Ackerman, T. P.: Tropical tropopause transition layer cirrus as represented by CALIPSO lidar observations, J. Atmos. Sci., 67, 3113–3129, doi:10.1175/2010JAS3412.1, 2010.

Wang, P.-H., Minnis, P., McCormick, M. P., Kent, G. S., and Skeens, K. M.: A 6-year climatology of cloud occurrence frequency from Stratospheric Aerosol and Gas Experiment II observations (1985–1990), J. Geophys. Res., 101, 29407–29429, doi:10.1029/96JD01780, 1996.

Wang, T. and Dessler, A. E.: Analysis of cirrus in the tropical tropopause layer from CALIPSO and MLS data: A water perspective, J. Geophys. Res., 117, D04211, doi:10.1029/2011JD016442, 2012.

Yamaguchi, T. and Randall, D. A.: Cooling of Entrained Parcels in a Large-Eddy Simulation, J. Atmos. Sci., 69, 1118–1136, doi:10.1175/JAS-D-11-080.1, 2012.